Colloids and Surfaces A: Physicochemical and Engineering Aspects 693 (2024) 134062

Contents lists available at ScienceDirect

Colloids and Surfaces A: Physicochemical and Engineering Aspects

journal homepage: www.elsevier.com/locate/colsurfa

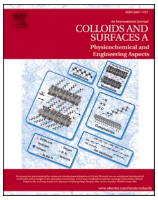

# Yield stress modification of suspensions of irregularly shaped particles by addition of spherical colloidal silica

Olivia Pickup [a], Leonard Turpin [b], Vyacheslav Kachkanov [b], Ria Mitchell [c], Martyn Barnes [d], Alexander Lockwood [d], Timothy N. Hunter [a], David Harbottle [a,*]

[a] School of Chemical and Process Engineering, University of Leeds, Leeds LS2 9JT, United Kingdom
[b] Diamond Light Source Ltd., Harwell Science and Innovation Campus, Didcot OX11 0DE, United Kingdom
[c] Sheffield Tomography Centre, The University of Sheffield, Sheffield S1 3JD, United Kingdom
[d] Particles with Fluids Centre of Expertise, Sellafield Ltd, Birchwood, Warrington, WA3 6GR, United Kingdom

## GRAPHICAL ABSTRACT

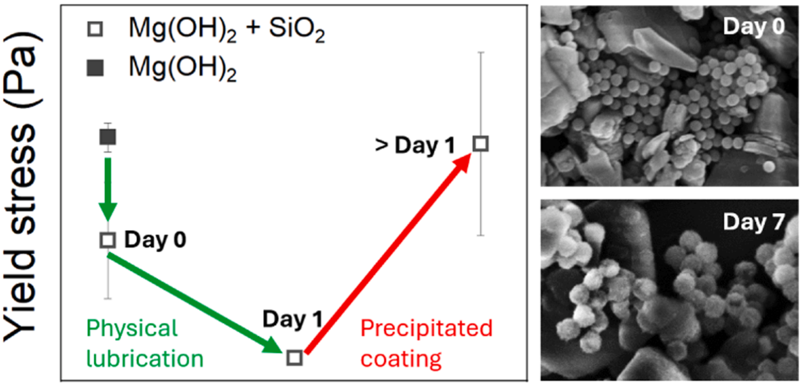

## ARTICLE INFO

*Keywords:*
Yield stress
Colloidal silica
Magnesium hydroxide
Magnesium silicate hydrate
Binary suspension

## ABSTRACT

Magnesium hydroxide ($Mg(OH)_2$) suspensions are encountered in the nuclear industry as legacy waste that is to be packaged for long-term storage. It is desirable to increase the solids content of the waste to minimize the total volume, yet this would produce high yield stress fluids that are difficult to process. However, high solids content suspensions of low yield strength are desired. Blending nano-silica (nano-$SiO_2$) into a high yield stress suspension of 27 vol% $Mg(OH)_2$, the suspension yield stress was reduced from 86 Pa to 47 Pa. X-ray CT imaging revealed that approximately two-thirds of the 3 vol% nano-$SiO_2$ added to the $Mg(OH)_2$ suspension was well-dispersed, with the rest forming large clusters that had minimal interaction with the $Mg(OH)_2$ network. SEM images showed small aggregates/individual particles of nano-$SiO_2$ dispersed between $Mg(OH)_2$ particles. We conclude that the finely dispersed nano-$SiO_2$ act like ball bearings to lubricate contacts between the irregularly shaped $Mg(OH)_2$ particles, thus decreasing yield stress. When aging the samples for several days, the yield stress of the binary suspension increased, reversing the yield stress reduction that was observed within the first day. The network stiffening is attributed to the formation of magnesium silicate hydrate (MSH) due to a reaction between soluble

---

* Corresponding author.
*E-mail address:* d.harbottle@leeds.ac.uk (D. Harbottle).

https://doi.org/10.1016/j.colsurfa.2024.134062
Received 23 January 2024; Received in revised form 19 April 2024; Accepted 21 April 2024
Available online 22 April 2024
0927-7757/© 2024 The Author(s). Published by Elsevier B.V. This is an open access article under the CC BY license (http://creativecommons.org/licenses/by/4.0/).

$Mg^{2+}$ and $Si(OH)_4$. The MSH precipitates onto the nano-$SiO_2$ to fuse particles together, thus reducing their effectiveness as flow modifiers. While this is a side effect of this particular binary suspension, the initial yield stress drop remains encouraging to provide the desired fluid conditions to process legacy wastes.

## 1. Introduction

Yield stress suspensions are ubiquitously encountered in the process industries as well as engineered/formulated products, including drilling fluids, cosmetics and agricultural formulations [1–3]. While yield stress fluids are often needed to deliver a particular product performance, it can also be an unwanted property that makes the handling and processing of such fluids more challenging. Legacy nuclear wastes are one particular example where a high yield stress fluid complicates the safe handling and long-term storage strategy of the waste [4].

Corroded Magnox fuel cladding on nuclear sites has consolidated to form high yield stress sediments that are undesirable as they can retain hydrogen [5–7], are challenging to retrieve from legacy containment vessels [8,9], and are difficult to process into new waste packages for long-term storage. Methods to reduce yield stress while maintaining a high solids content are highly desired to improve processability but also minimize the total volume of waste that will be stored long-term. Selecting appropriate additives to modify suspension rheology is challenging because of incompatibilities between the waste and organic flow modifiers. Therefore, the study has considered the use of spherical silica as a flow modifier.

Highly concentrated suspensions of metal oxides can exhibit a variety of flow properties, which often depend on the interaction strength between colloidal particles [10–13]. By modifying the particle surface potential, the electrostatic interaction between colloids is modulated, and can be adjusted from strongly attractive at the iso-electric point, where the suspension yield stress approaches a maximum, to strongly repulsive where the suspension can be Newtonian-like in behavior [10]. Furthermore, the effect of modulating yield stress by adjusting the electrostatic interaction is more apparent when the occupied volume of the suspension is increased, either by adding more solids, or caused by low particle sphericity which has the effect of increasing the apparent solids volume fraction. Several studies have shown that the yield stress dependency on solids volume fraction scales as a power-law [12,14,15], with particle shape affecting the maximum packing fraction [16]. While this method of flow modification is well-established, it is not an option to treat $Mg(OH)_2$ suspensions because of their low surface potentials across a range of pHs, and its natural buffering to the iso-electric point [17].

Alternatively, flow modification can be achieved by adding polymers and/or surfactants to the colloidal suspension, modifying not only the electrostatic forces but also introducing steric repulsive forces between neighboring particles [18–20]. The latter being an effective way of modifying rheology in organic solvents where electrostatic forces are significantly weakened. However, as previously mentioned, organics can cause substantial incompatibility issues when blended with legacy nuclear wastes, and hence are considered undesirable as they may impact the cement hydration reaction and reduce the lasting durability of the waste containment [21,22].

Binary or bidisperse suspensions have received significant scientific attention because of their challenging contact mechanics, as well as them being more relevant to industrial systems, in particular the processing of ceramics. Cerbelaud and co-workers published a series of computational and experimental studies on the heteroaggregation of alumina and silica particles [23–26]. With weak electrostatic attraction between the dissimilar colloids, their mutual interaction modified the apparent surface potential of alumina, thus altering the suspension stability. The authors showed that for particles of a similar size, those aggregates were more fractal-like, but aggregates could be made more compact by increasing the size ratio between the two species. For smaller sized silica, the large alumina particles were partially coated by silica, noting that the overall surface coverage was significantly below that of a close-packed layer, with surface coverage limited by repulsions between the silica particles. Even so, the low surface coverage was sufficient to induce changes in suspension stability and viscosity, with suspension viscosities remaining low for high loading ratios of silica, which might be expected since the system is likely dominated by interactions between the silica particles, something similar to the work of Singh et al. [27]. who discussed the changing contact mechanics in bidisperse non-Brownian suspensions. By increasing the volume ratio ($\alpha$) of small particles within the non-Brownian suspension, the authors observed both a decrease (for low $\alpha$, up to $\alpha \sim 0.5$) and increase (for $\alpha \rightarrow 1$) in the relative viscosity. This behavior was attributed to the stress contributions of each particle type, shifting from predominately large-large contacts at small $\alpha$, to small-small contacts at large $\alpha$.

Fisher et al. [28] studied the viscosity of similar alumina-silica suspensions but focused on the effect of particle size ratio. For similar sized particles, adding silica to the alumina suspension increased its viscosity, with the effect attributed to interparticle attraction. However, by increasing the size ratio (adding smaller silica particles), the suspension viscosity could be lowered eventually exhibiting Newtonian-like behavior. The authors attributed such behavior to the shifting iso-electric point of the alumina as it is increasingly coated by the nanoparticles, with the authors commenting that close-packed coverage of silica is needed to achieve the minimum viscosity. While the reduced viscosity is apparent, the interpretation of a shifting iso-electric point of a binary suspension is difficult to assess from zeta potential measurements [29]. This is also similar to the theory proposed by Zhu et al. [30], except it was extended to include steric effects caused by the adsorbed silica. Reduced viscosities were also reported by Kong et al. [31], but interestingly their observations appear to contradict the idea of silica nanoparticles coating the alumina to modify its apparent surface potential. TEM imaging of a dried alumina particle showed few silica particles, hence the authors proposed a nanoparticle 'halo' mechanism to account for the modified viscosity. This is different to other mechanisms as the basis for the 'halo' model is non-interaction between the silica and alumina particles, thus the reduced viscosity is predominantly affected by silica-silica interactions.

Shape effects of the secondary component were explored by ten Brinke et al. [32], who characterized the rheology of 2.5 wt% hectorite clay dispersions in the presence of rod, platelet and spherical nanoparticles. With a strong attractive interaction potential between the two particle types (hectorite clay and secondary particle), the authors observed increased rheological parameters (G', G", $\tau_y, \eta_{\tau \rightarrow 0}$), with the magnitude of those changes depending on particle shape. Spherical particles formed the strongest and most fragile gels, which the authors speculated was due to the particles being able to pack more efficiently between and thus bridging hectorite particles. However, since those comparisons were made for equivalent mass fractions, the authors did note that the number of spherical particles was significantly greater than the platelet- and rod-shaped particles, potentially screening some of the effects of particle shape.

Although there is significant interest in bidisperse suspensions, particularly for rheology and stability control, the mechanism to induce those changes remains to be debated. We studied bidisperse suspensions of $Mg(OH)_2$ (major component) and nano-$SiO_2$ (minor component), with the aim of lowering the yield stress of concentrated $Mg(OH)_2$ by achieving good dispersion and distribution of the nano-$SiO_2$ throughout the $Mg(OH)_2$ network. At the test conditions there is weak attraction between the two particle types, and when adding $SiO_2$ at an approximately equivalent number ratio to that of $Mg(OH)_2$, a significant reduction in the yield stress was measured. Because of the limited number of $SiO_2$ particles, we did not observe the coating of $Mg(OH)_2$ particles by $SiO_2$ particles, thus electrostatics and 'haloing' would not be a factor here, nor would a changing stress contribution in the particle network, since the $SiO_2$ particles were sparsely dispersed. However, high-resolution imaging revealed the nano-$SiO_2$ to embed between Mg $(OH)_2$ particles, suggesting that the spherical particles act as ball bearings to enable mobility of the irregularly shaped $Mg(OH)_2$ particles under an applied stress. The study provides new insights into rheological modification of bidisperse suspensions, and highlights that such changes can be achieved with very few secondary particles present in the suspension.

## 2. Materials and methods

Magnesium hydroxide (Versamag®, Martin Marietta, US) powder with a MgO content <1 % and particle density of 2.36 g/cm$^3$, and amorphous colloidal silica (AngstromSphere, Fiber Optic Center, US) with a particle density of 1.88 g/cm$^3$ were used as received. SEM images of the two particle types are provided in Fig. S1 of the Supporting Information showing the colloidal silica is spherical and approximately monodispersed, while the $Mg(OH)_2$ particles are larger, irregularly shaped and more polydisperse. All suspensions were prepared in $10^{-3}$ M NaCl electrolyte solution at pH 9.6, with 1 M HCl or 1 M NaOH used to adjust the pH. At these conditions the zeta potentials of magnesium hydroxide ($Mg(OH)_2$) and silica ($SiO_2$) were 5.4 mV and − 40 mV, respectively, measured using the Zetasizer Advance (Malvern Panalytical, UK). The method and zeta potential vs pH dependence are shown in the Supporting Information, Fig. S2. Using the same instrument, the $SiO_2$ $d_{50}$ was 102 nm, and the $d_{50}$ of $Mg(OH)_2$ was 5.4 µm, measured using the Mastersizer 3000 (Malvern Panalytical, UK).

### 2.1. Sample preparation

Suspensions of $Mg(OH)_2$ were prepared by gradually adding the required mass of $Mg(OH)_2$ powder to 50 mL of $10^{-3}$ M NaCl while stirring at 600 rpm (Compact mixer, Cole Parmer) using a 30 mm four-blade impeller. After mixing for 10 min the sample was transferred to an orbital shaker (Stuart SSL1) and agitated overnight. A similar procedure was followed to prepare the dilute $SiO_2$ suspensions, except the suspensions were tip-sonicated for 10 min prior to gently agitating overnight. After 24 h the $SiO_2$ suspension was sonicated for 10 min before being added dropwise to the $Mg(OH)_2$ suspension while being stirred at 800 rpm. The binary suspension was agitated for a predetermined amount of time prior to measuring its yield stress.

### 2.2. Rheology

A DHR-2 rheometer (TA Instruments, UK) with a vane geometry (D: 15 mm, L: 38 mm) and sand blasted cup (D = 29.2 mm) was used to measure the suspension yield stress. The choice of geometries was made to minimize any effects of wall slip [33]. Prior to use, the standard instrument setup and calibration procedures were followed, with the geometry gap set to 8800 µm. After setup, 40 mL of the mixed suspension was poured into the cup and the vane lowered to the gap position. Although not needed due to the short measurement time, the solvent trap was added to minimize any effect of surface drying. It should be noted that the aged suspensions were not pre-sheared as the aim was to measure the effects of aging. The suspension yield stress was measured using a linear stress ramp protocol which included an equilibration time of 200 s, followed by increasing the decreasing the shear stress between 0 and 200 Pa without any hold time. For each cycle, 600 data points were collected at a rate of 1 point/s. The yield stress was determined from the Bingham model fitting at the incipient point of increasing shear rate [34].

### 2.3. Quartz crystal microbalance

The time-dependent stiffening (yield stress growth) of the binary particle suspension was measured using a dip-probe quartz crystal microbalance (QCM) (SRS QCM200, US). A 5 MHz gold-coated AT-cut quartz sensor was cleaned by sonicating in 2 vol% Decon-90 solution, then rinsed with Milli-Q water before drying with nitrogen gas. With the sensor mounted in the holder, a stable baseline (< 5 Hz/h) in air was established by allowing the sensor to run for ~30 min. The sensor was then fully submerged in 50 mL of suspension and the sample beaker rotated to ensure good contact between the sample and sensor. A thin layer of mineral oil was added on top of the suspension and the sample beaker sealed with Parafilm to avoid sample drying. The sample beaker with QCM was then placed in a water bath maintained at 30°C. The instrument capacitance was adjusted to 'null' so that the frequency and resistance values corresponded to the true series resonant parameters of the quartz oscillator. The sensor resonance properties were then measured for 40 h.

### 2.4. Thermal analysis

A combined thermogravimetric analyzer and differential scanning calorimeter (TGA/DSC Simultaneous Thermal Analysis, Mettler Toledo, US) was used to detect the presence of magnesium silicate hydrate (MSH) in aged suspensions. The aged suspensions were gently mixed before sampling 45 – 60 mg to be loaded into an alumina crucible. The heat ramp was from 30 to 1000°C at 10 °C/min with a flow of nitrogen gas over the sample. Both the heat flow (mW) and mass change (mg) were simultaneously measured.

### 2.5. UV–visible spectroscopy

The concentration of dissolved silica was measured using UV–visible spectroscopy (Cary 60, Aligent Technologies, US). The method used was adapted from Yang et al. [35]. Mixed suspensions were prepared and aged as previously described and then centrifuged at 9000 rpm for 20 min to recover the supernatant. The supernatant was then syringe filtered (250 nm pore size), pH adjusted to pH 2 using 1 M HCl, and diluted (1:1 vol ratio) with Milli-Q water. 25 mL of the sample was reacted with 1.5 mL of 7.5 % ammonium molybdate solution to form a weakly yellow Mo(VI) complex (Eq.1). Tartaric acid (4 mL, 10 mol%) was added before reducing to the silico-molybdenum blue complex containing Mo(VI) and Mo(V) with 1 mL of a pre-mixed reducing solution which consisted of 4-amino 3-hydroxynaphthalene 1-sulfonic acid (0.15 g), sodium sulphite (0.7 g) and sodium hydrogen sulphite (20 mL, 45 mol%) in Milli-Q water (100 mL). After adding all reagents the solutions were left for 1 h before adding 3.5 mL to a quartz cuvette and measuring the UV–visible absorbance spectrum between 200 and 800 nm. The peak absorbance at 680 nm was measured and the dissolved silica concentration determined using a calibration line (Fig. S4) based on a silica standard (32.09 mg/L, Fisher Scientific).

The proposed reactions are as follows, adapted from Strickland[36] and Nagul et al. [37]:

$$SiO_4{}^{4-} + 12[MoO_4{}^{2-}] + 28H^+ \rightarrow H_4SiMo_{12}O_{40} + 12H_2O \quad (1)$$

$$H_4SiMo_{12}O_{40} + reducing \quad agent \rightarrow [H_5SiMo_8^{6+}Mo_4^{5+}O_{40}]^{3-} \quad (2)$$

where $H_4SiMo_{12}O_{40}$ is a yellow Mo(VI) complex that is partially reduced by $SO_3^{2-}$ anions in the reducing agent to form the blue Mo(V)/Mo(VI) complex in Eq. 2.

### 2.6. Imaging

Scanning electron microscope (SEM) images of the binary suspensions were taken using a Nova 450 NanoSEM, (FEI, US). A voltage of

3 kV was used with an ideal resolution of 0.78 nm and magnification range between 100× – 750,000 × .

Both laboratory-based and synchrotron X-ray computed tomography was used to image the larger $SiO_2$ clusters distributed throughout the suspension non-destructively in 3D.

*Synchrotron at Diamond Light Source (Didcot, UK)*: On beamline I13–2 a pink beam centred around 27 keV was used and filtered using a 140 μm thick Fe filter and a 20 μm thick Ni foil to stop the sample from boiling. The projections were acquired using a PCO edge 5.5 camera with 4× magnification resulting in a pixel size of 1.625 μm and a 4.2 × 3.5 mm field of view. Binary suspensions were prepared following the standard procedure and 1.5 mL was subsampled and sealed in a polypropylene tube (Eppendorf Tubes® 3810X) to be mounted on the tomography stage. The exposure time for each projection was 0.2 s, with a total acquisition time of 13 min. The tomographic reconstructions were performed using Savu 3.0 processing pipeline [38]. Post-processing of the images was done using the Avizo 2022.1 Software (ThermoFisher Scientific, USA). A sub-volume of the full scan volume was taken (2066 × 2323 × 3413 $\mu m^3$) and a series of image filters were applied before threshold segmentation of $SiO_2$ enabled cluster volumes $\geq 1 \times 10^5$ $\mu m^3$ to be isolated for volume analysis.

*Laboratory-based X-ray tomography at Sheffield Tomography Centre:* $SiO_2$ clusters were imaged using a ZEISS Microscopy (Germany) Xradia Versa 620 X-ray Microscope (XRM). Subsamples of the suspension (0.06 mL) were syringed (15 G) into Kapton polyamide tubing (i.d. = 1.8 mm, L = 25 mm, wall thickness 0.05 mm) which was sealed and mounted onto an aluminium pin (w = 1.5 mm, L = 30 mm) for imaging. X-ray source conditions of 80 kV, 90 μA and 4 W was used with a 4 × objective lens that provided a field of view of 3047 $\mu m^2$ and a 3 μm voxel size. The sample was scanned in four sections each of 801 projections that were then automatically stitched together to provide an image of the whole tube length. The total scan time for each sample was 2.25 h. The reconstructed images were post processed using ORS Dragonfly software (Version 2020.2, Object Research Systems (ORS) Inc, Montreal, Canada, 2020). A cylindrical volume of length 3.55 mm and radius 0.88 mm was extracted from the centre of the scan which allowed thresholding and segmentation of $SiO_2$ clusters using Dragonfly's multi-ROI tool. The clusters were isolated at volumes $\geq 1.2 \times 10^{-5}$ $mm^3$ and colour coded to represent the different cluster volumes.

## 3. Results and discussion

### 3.1. Suspension yield stress

Yield stress is the critical stress which is to be exceeded to initiate flow. For particle suspensions, the yield stress depends on the number of particle contacts and the interaction strength between those contacts, which for colloidal particles is modified by the balance between attractive (van der Waals) and dispersive (electrical double layer) forces. In a binary suspension of two particle types, the total interaction energy ($V_T$) between two dissimilar particles can be approximated by the Hogg-Healy-Fuerstenau (HHF) equation (summation of Eqs. 3 and 4), where Eq. 3 describes the electrostatic repulsive forces and Eq. 4 the van der Waals attractive forces [39]. The differences between the two particle types are accounted for by the particle radius (a), surface potential ($\psi$) and Hamaker constant (A):

$$V_R = -\frac{\pi\varepsilon_0\varepsilon_r a_1 a_2}{(a_1+a_2)}\left(2\psi_1\psi_2\ln\left[\frac{1+e^{-\kappa H}}{1-e^{-\kappa H}}\right]+\left({\psi_1}^2+{\psi_2}^2\right)\ln\left[1-e^{-2\kappa H}\right]\right) \tag{3}$$

$$V_A = -\frac{A_{123}}{6H}\frac{a_1 a_2}{(a_1+a_2)} \tag{4}$$

where $\varepsilon_0$ is the permittivity of free space, $\varepsilon_r$ the permittivity of the medium, κ the inverse Debye length, and H the particle-particle separation distance.

Considering the two particle types, $SiO_2$ and $Mg(OH)_2$, the interaction potential between $SiO_2$-$SiO_2$ at pH 9.6 in $10^{-3}$ M NaCl is calculated to be repulsive (Fig. 1a) due to the high surface potential (-40 mV) of $SiO_2$ at those conditions. However, with no reported Hamaker constant value for $Mg(OH)_2$, the theoretical interaction potential could only be approximated by considering the properties of MgO. For MgO-MgO, the interaction potential at those same conditions is strongly attractive (Fig. 1a), caused by the low surface potential (+5 mV) and strong van der Waals forces due to the Hamaker constant. For the mixed system $SiO_2$-MgO, the interaction potential is weakly attractive and occurs over a much shorter separation distance than seen for MgO-MgO. Hence, for the binary particle suspensions the interaction potential between the two particle types decreases in the following order: MgO-MgO > $SiO_2$-MgO > $SiO_2$-$SiO_2$. Therefore, the HHF theory suggests that the $SiO_2$ particles should be readily dispersed and therefore easier to distribute throughout the network of aggregated $Mg(OH)_2$ particles.

Dynamic light scattering of $Mg(OH)_2$ and $SiO_2$ particles at the test conditions was qualitatively used to verify those differences in the aggregated-state of the two particle types. For $SiO_2$, the $d_{50}$ particle size was almost the same as the primary particle size (~102 nm), while for $Mg(OH)_2$ the $d_{50}$ was almost 20 times larger than the primary particle size of ~250 nm, see Fig. S3 of the Supporting Information. Due to difficulties in measuring the primary particle size of $Mg(OH)_2$ by dynamic light scattering (highly aggregated and irregular shape), the primary particle size ($d_{prim}$) was approximated from the particle specific surface area (SSA, $m^2/g$) and density (ρ, $g/cm^3$) by $d_{prim}(nm) = \frac{6000}{SSA\bullet\rho}$, which assumes a size based on the equivalent spherical diameter[40].

After mixing the minor component ($SiO_2$ suspension) into the $Mg(OH)_2$ suspension, sub-millimeter sized clusters of $SiO_2$ were found to be distributed throughout the binary suspension, see Fig. 2a for the X-ray CT image of the $Mg(OH)_2$ + $SiO_2$ suspension prepared to 27:3 vol%:vol%. Reconstructing the 3D image (Fig. 2b) reveals a significant number of silica clusters distributed throughout the suspension, even though the sample preparation method had been optimized such that the volume base particle size distribution had a $d_{50}$ of 102 nm. Fig. 2b shows silica clusters larger than $1 \times 10^5$ $\mu m^3$, and hence there is a fraction of the added silica that is below the threshold. A simple calculation based on the measured occupied volume of silica (assuming closed packed spheres) and the initial silica volume fraction suggests that approximately 62 % of the added silica is well dispersed (below the volume threshold) throughout the $Mg(OH)_2$ suspension. SEM imaging was able to reveal those smaller silica clusters and even single silica particles distributed throughout the $Mg(OH)_2$ suspension (Fig. 1b). The SEM image also confirms that the $SiO_2$ particles do not fully coat the $Mg(OH)_2$ particles, but are more randomly distributed on the surface of a few $Mg(OH)_2$ particles, as well as positioning in the void spaces between the larger $Mg(OH)_2$ particles.

Although adding the nano-sized silica to the $Mg(OH)_2$ suspension increases the total solids volume fraction (27–30 vol%), the binary suspension had a substantially lower yield stress compared to the $Mg(OH)_2$ suspension, 47 Pa compared to 86 Pa (Fig. 2c). As discussed earlier, the proposed mechanisms for rheological modification are often attributed to changes in the electrostatic interactions (induced by particle coatings), 'haloing' the larger particles by smaller particles, or changing the stress contribution within the particle network [28,30,31]. Since these mechanisms rely on the smaller particles surrounding the larger particles, or a significant network of the smaller particles being formed within the suspension, such mechanisms would not be relevant to our observation. From the high-resolution image (Fig. 1b) we see the $SiO_2$ particles to be sparsely dispersed, with the nano-$SiO_2$ embedded between $Mg(OH)_2$ particles, suggesting that the spherical particles act as ball bearings to enhance mobility of the irregularly shaped $Mg(OH)_2$ particles under an applied stress. Although the data is not shown here, when adding other dispersed non-spherical nanoparticles to the $Mg(OH)_2$ suspension such as $TiO_2$, $BaSO_4$, $CeO_2$ and $ZrO_2$, the yield stress of

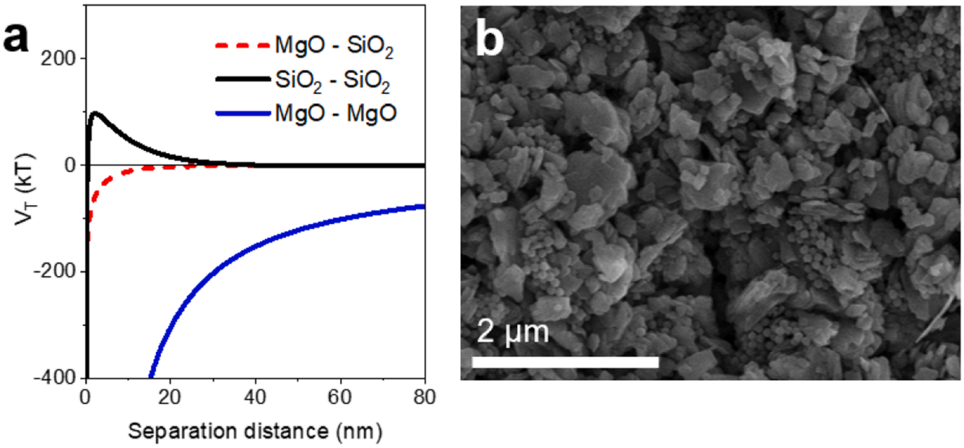

**Fig. 1.** Total interaction potential approximated using the HHF theory (a). The Hamaker constants used were: i) MgO–MgO, $A_H = 1.21 \times 10^{-19}$ J; ii) $SiO_2$–$SiO_2$, $A_H = 6.5 \times 10^{-20}$ J; and iii) MgO − $H_2O$ − $SiO_2$, $A_{132} = 9.73 \times 10^{-21}$ J. The zeta potentials were +5 mV for $Mg(OH)_2$ and −40 mV for $SiO_2$. SEM micrograph of the binary suspension of $Mg(OH)_2$ and $SiO_2$ prepared to 27:3 vol%:vol% (b).

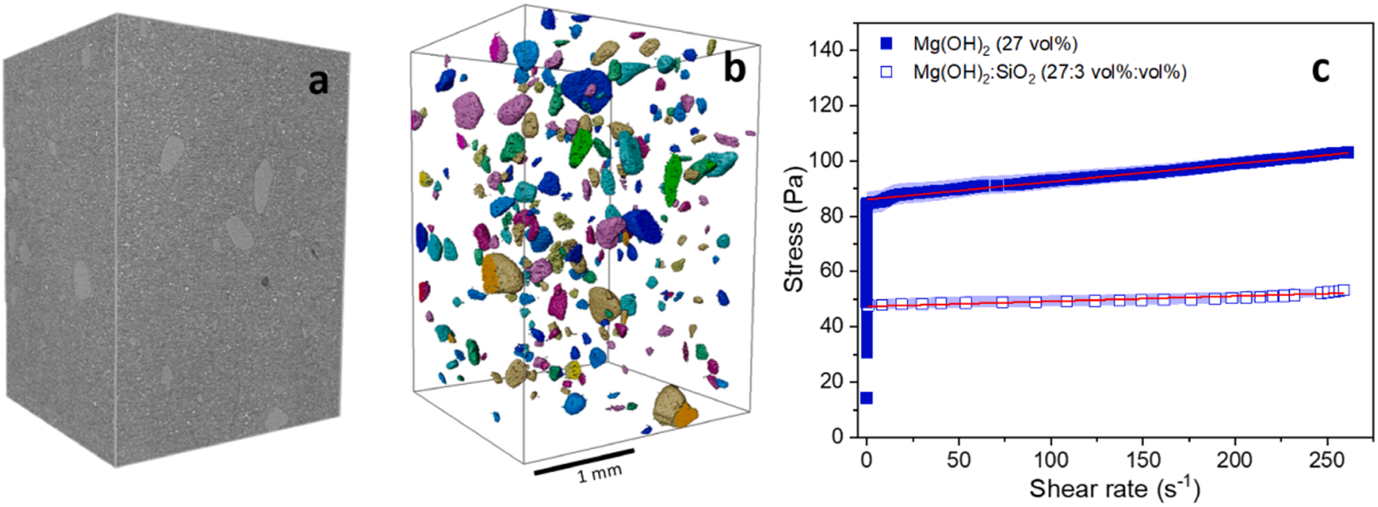

**Fig. 2.** Binary suspension of $Mg(OH)_2$ and $SiO_2$ (27:3 vol%:vol%) imaged by synchrotron X-ray CT (a). Segmented X-ray CT volume highlighting $SiO_2$ clusters with a volume greater than $1 \times 10^5$ μm$^3$ (b). Upwards stress ramp of $Mg(OH)_2$ and $Mg(OH)_2$:$SiO_2$ suspensions (c), solid lines are the Bingham model fittings: $Mg(OH)_2$, $\sigma_y = 86$ Pa and $\eta_B = 0.06$ Pa.s; $Mg(OH)_2$:$SiO_2$, $\sigma_y = 47$ Pa and $\eta_B = 0.01$ Pa.s.

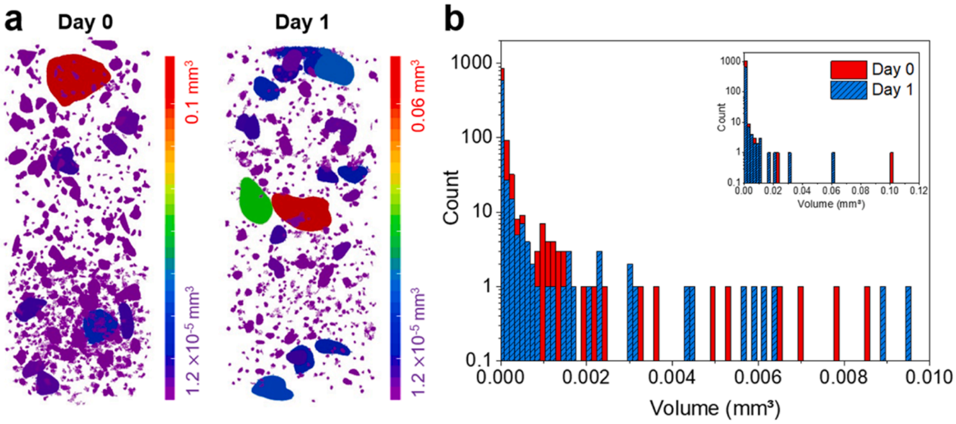

**Fig. 3.** Segmented laboratory X-ray CT volume analysis of the binary suspension ($Mg(OH)_2$ and $SiO_2$, 27:3 vol%:vol%) imaged on Day 0 and Day 1 (a). The images show $SiO_2$ clusters with a volume greater than $1.2 \times 10^{-5}$ mm$^3$. Number and volume base size of $SiO_2$ clusters in the Day 0 and Day 1 samples (b). Inset shows the full volume range.

the binary suspension did not change. Hence, particle shape, more specifically particle sphericity, appears critical to the observed effect, and further supports the idea that the mechanism to lower yield stress is akin to ball bearings reducing contact friction.

### 3.2. *Suspension aging*

Although the yield stress of the $Mg(OH)_2$ suspension can be lowered when adding nano-$SiO_2$, the binary suspension yield stress was found to be time-dependent and would increase if left for prolonged periods of time, see Fig. 4. Such aging could be attributed to the stiffening of the $Mg(OH)_2$ network, which has been shown to result from dissolution of the MgO content at high pH (MgO content of the Versamag® sample = 1 wt %), and its subsequent hydration to $Mg(OH)_2$ which then re-precipitates onto the particle network, stiffening contacts and increasing yield strength [41]. However, the aging effect seen for the binary suspension is more severe than the $Mg(OH)_2$ suspension, suggesting another factor more significantly influences yield stress growth.

During the first 24 h the yield stress of the binary suspension decreased. X-ray CT images (Fig. 3a) of the same sample imaged immediately after preparation and one day later showed that the number of large silica clusters appeared to decrease slightly (Fig. 3b). Recognizing that this is a small dataset, and being careful not to over interpret the images, the reduced cluster size may suggest better dispersion of the nano-$SiO_2$ particles, which would be favorable to reduce yield stress based upon the proposed mechanism. Furthermore, gentle agitation of the sample could better distribute nano-$SiO_2$ throughout the $Mg(OH)_2$ network, again increasing the number of dissimilar contacts which would also promote a reduced yield stress. Although it is not possible to say which mechanism contributes most to this time-dependency, it is likely that both effects (particle distribution and dispersion) enhance the yield stress reduction.

After Day 1 the yield stress increased for both the unagitated and agitated binary suspensions, with both suspensions having at yield stress that exceeded that of the 27 vol% $Mg(OH)_2$ suspension after Day 7, see Fig. 4. Although both suspensions exhibited yield stress growth, the effect was more severe in the unagitated sample, suggesting that the mechanism for yield stress growth is partly disrupted when the sample is continually agitated. It is worth noting that the higher error for the Day 5 measurements of the unagitated samples is a consequence of the high yield stress and the absence of a sample pre-shear in the test method. A pre-shear would normally be run to nullify any effects of sample history, but for this study those sample history effects are important to measure.

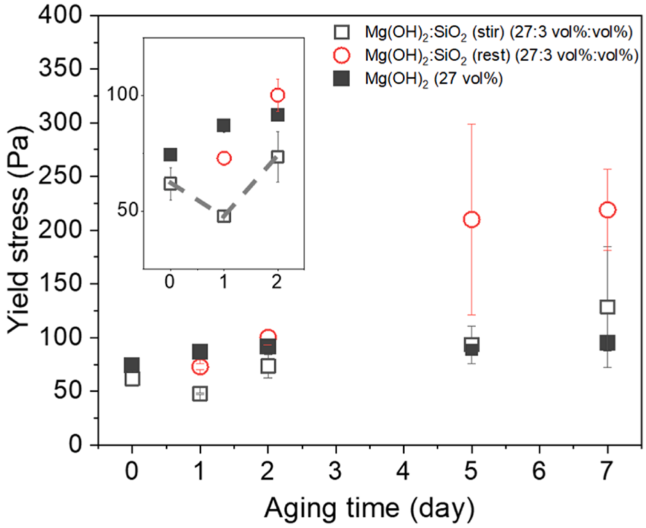

**Fig. 4.** Yield stress of the $Mg(OH)_2$ and binary ($Mg(OH)_2$ and $SiO_2$, 27:3 vol%:vol%) suspensions as a function of aging time at ambient conditions.

The yield stress growth in the unagitated suspension ($Mg(OH)_2$ + $SiO_2$ at 27:3 vol%:vol%) was verified using the QCM technique. This is a method we have previously used to monitor yield stress changes in $Mg(OH)_2$ suspensions, with further details of the method provided in Botha et al. [41]. With the QCM sensor submerged in the sample, the resonance frequency ($\Delta F_1$) and resistance ($\Delta R_1$) were continuously measured (Fig. 5a), and the differential loss tangent ($\frac{\Delta\Gamma}{\Delta F_1}$), where $\Delta\Gamma \sim 2\ \Delta R_1$, plotted as a function of time, see Fig. 5b. Here, $\Delta\Gamma$ is a measure of the material losses (i.e. viscous dampening), and $\Delta F_1$ a measure of the material stiffness. Therefore, a decreasing ratio of $\frac{\Delta\Gamma}{\Delta F_1}$ confirms the particle network to be stiffening.

Fig. 5a shows that for water the resonance properties of the sensor remain unchanged over 40 h, confirming its good resonance stability. However, for the binary suspension both the resonance frequency and resistance increase with time. The differential loss tangent shows three distinct regions as the suspension ages (Fig. 5b). Region I (0 – 10 h) has a $\frac{\Delta\Gamma}{\Delta F_1}$ slope of 2.5, indicating that the suspension is becoming more lossy, likely reflecting the yield stress decrease immediately following mixing of silica with $Mg(OH)_2$. Then, Region II (10 – 18 h) has a reduced slope of 1.1, and in Region III (> 18 h) the slope is reduced further to 0.6. Regions II and III confirm that the particle network is stiffening which is in good agreement with the findings from the yield stress measurements. It is worth noting that the sample is undisturbed in the QCM test and so the data cannot be influenced by sample handling, yet the response is characteristic of those yield stress changes seen in Fig. 4, where yield strength initially reduces before a period of prolonged particle network stiffening.

The prolonged stiffening of the particle network can be better understood by considering the dynamically changing surface and aqueous chemistries in alkaline conditions. At pH > 9 the surface hydroxyls of $Mg(OH)_2$ are in equilibrium as follows: $Mg(OH)_{2(s)} \rightleftharpoons Mg^{2+}{}_{(aq)} + 2OH^-$. However, at high pH the rate of dissolution of colloidal silica increases, forming silicic acid ($Si(OH)_4$) due to hydrolysis of the silicon-oxygen bonds. The acid lowers the solution pH and shifts the reaction equilibrium of $Mg(OH)_2$ to release more $Mg^{2+}_{(aq)}$ and $OH^-$ to counteract this, thus accelerating the reaction further and creating ongoing fluctuations in pH [42].

The amount of dissolved silica in the suspension liquor was measured using UV–vis (Fig. 6a). During the initial phase of sample aging (Day 0 to Day 3) the peak absorbance was high and increased slightly, confirming a high concentration of dissolved silica in the aqueous phase. After Day 3 the concentration slightly reduced up to Day 7, before being almost depleted at Day 14. The data suggests that initially there is an abundance of aqueous Si that is able to complex with $Mg^{2+}{}_{(aq)}$, but with aging the rate of complexation decreases due to the low reactant concentration. With the particle number ratio in the binary suspension being 1–2 ($Mg(OH)_2$ to $SiO_2$), and the specific surface areas of the two particle types being 10.22 $m^2/kg$ for $Mg(OH)_2$ and 2–6 $m^2/kg$ for $SiO_2$, the reduced concentration of aqueous Si cannot be attributed to the lack of available silica, but likely results from another mechanism that limits its dissolution.

DSC analysis of samples aged for significantly longer periods of time identified two endothermic peaks (Fig. 6b), the first associated with the loss of free water and the second being the decomposition of $Mg(OH)_2$, as well as one smaller exothermic peak at ~850 °C which has been attributed to the crystallisation of amorphous magnesium silicate hydrate (MSH) into $MgSiO_3$ [43,44]. With no exothermic peak measured in the Day 3 sample, suggesting either the absence of very low concentration of MSH, with prolonged aging (1 and 6 months) the MSH peak is measurable. The enthalpies of those transitions are 70 J/g and 78 J/g for the 1-month and 6-month samples respectively, suggesting that MSH is rapidly formed within the first month (maybe shorter than one month) and changes thereafter are negligible, in good agreement with the UV–vis findings.

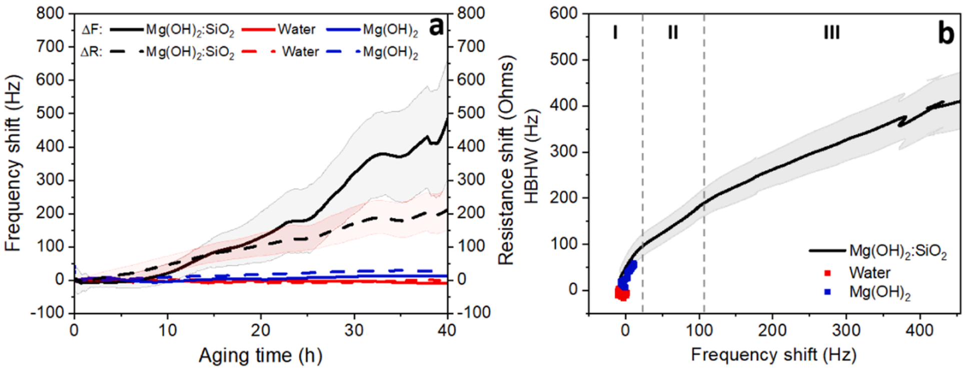

**Fig. 5.** Time dependent frequency and resistance responses of the QCM submerged in water, $Mg(OH)_2$ and binary ($Mg(OH)_2$ and $SiO_2$, 27:3 vol%:vol%) suspensions (a). Differential loss tangent ($\Delta\Gamma/\Delta F$) with sample aging showing the binary suspension to have three distinct regions of aging: Region I $\Delta\Gamma/\Delta F = 2.5$, $R^2 = 0.99$; Region II $\Delta\Gamma/\Delta F = 1.1$, $R^2 = 0.99$; and Region III $\Delta\Gamma/\Delta F = 0.6$, $R^2 = 0.99$ (b).

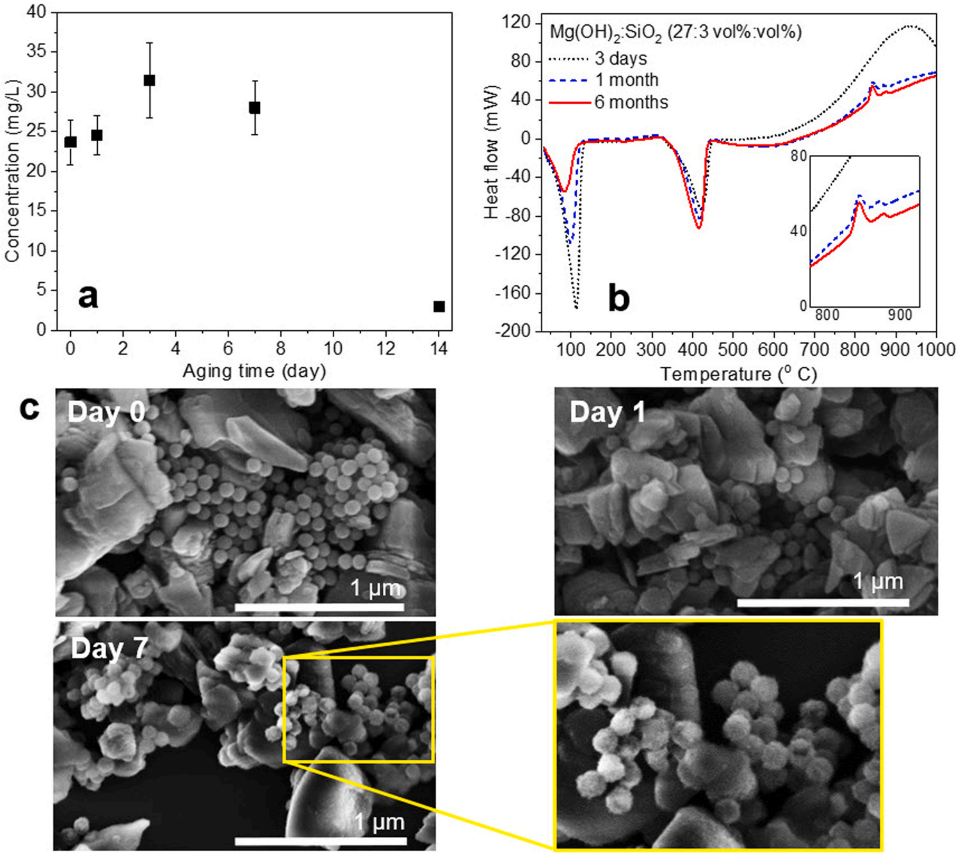

**Fig. 6.** Chemical characterisation of the aqueous and solid phases during aging of the binary suspension, $Mg(OH)_2$ and $SiO_2$, 27:3 vol%:vol%. Dissolved silica concentration measured by UV–vis (a); Thermal analysis of aged binary suspensions confirming the presence of MSH in the one and six month samples (b); SEM images of the same sample aged for seven days (c). The expanded region highlights the roughening of the silica particles due an MSH coating that fuses together the colloidal particles.

Although not measurable by DSC, high resolution SEM imaging suggests that MSH is forming within the first seven days (Fig. 6c). Samples collected from the Day 0 and Day 1 suspensions show particles with defined edges and particle surfaces that appear visually smooth. However, after aging for seven days those defined edges are no longer visible, with both particles (more specifically the silica particles) appearing significantly roughened, and even fused together. Dewitte et al. [45] described the formation of MSH as “globular chains”, and Zhang et al. noted that with longer aging times MSH forms a shell around the slowly dissolving silica particles [46]. Our findings appear consistent with those studies and confirm that the formation of precipitated MSH hinders the ongoing dissolution of silica, as well as acting to fuse together the nano-$SiO_2$, and possibly the $Mg(OH)_2$ and nano-$SiO_2$ particles. Even though the silica particles become less spherical, such change is not thought to contribute to the increased yield stress (Fig. 4), which is more likely affected by the MSH binding particles together. Further support for MSH binding is that yield stress growth was less severe when gently agitating the sample, thus particle-particle contacts are continually disrupted and the formation of a coating to fuse particles together is less likely to form. This would agree with other studies that

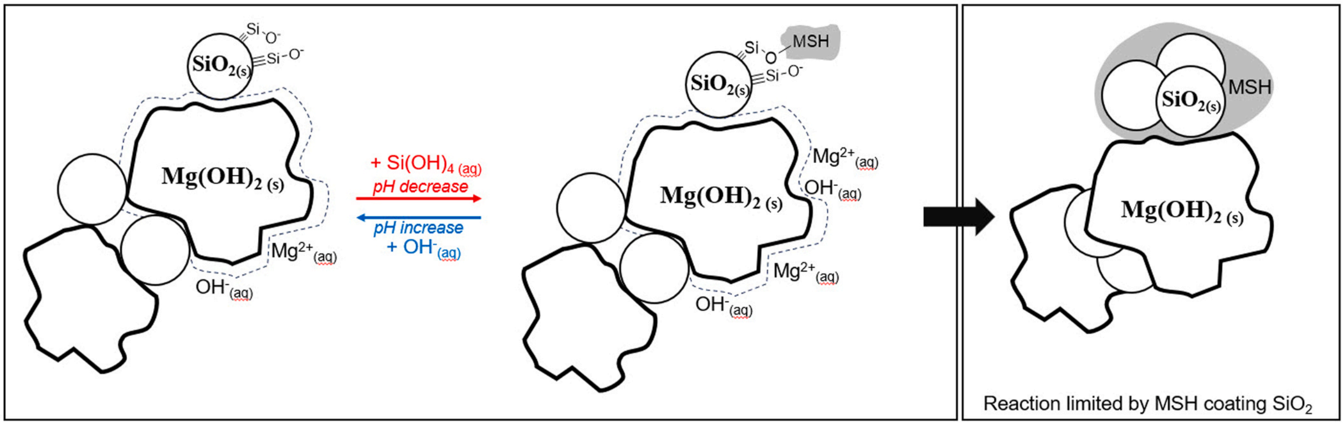

**Fig. 7.** Schematic highlighting the mechanism by which the changing aqueous and solid surface chemistry leads to the formation of magnesium silicate hydrate (MSH) which causes the yield stress of the binary suspension to increase.

suggested that MSH "bridges" can be broken when sheared [47], and reformation of the coating led to weaker binding of the particles [48].

The mechanism for yield stress growth is shown in Fig. 7. With the suspension pH at 9.6 there is an amount of $Mg^{2+}$ in solution that is in equilibrium with $Mg(OH)_2$. This equilibrium is then shifted as the colloidal silica dissolves to form $Si(OH)_4$, reducing the solution pH and releasing more $Mg^{2+}$ as well as $OH^-$ which slightly stabilizes the solution pH. It is worth noting that the suspension pH decreased from pH 9.6–9 between Day 0 to Day 3. The $Si(OH)_4$ and $Mg^{2+}$ complex to form a MSH gel that consumes the dissolved species which are then replaced due to an excess of accessible surface groups. The MSH gel is able to bind with the polar groups on the $SiO_2$ surface, forming a coating that reduces accessible surface groups and begins to inhibit further dissolution of $SiO_2$ [49]. With aging the ionic composition of the solution changes, varying the stoichiometry which effects the composition of the MSH gel, likely forming different magnesium silicate structures [50,51]. Eventually the accessible $SiO_2$ surface sites are shielded by the MSH coating, and its ongoing formation is significantly hindered. As the MSH gel coats the nano-$SiO_2$ surface it fuses particles together, reducing their effectiveness as flow modifiers, but also strengthens particle-particle contacts which promotes yield stress growth.

## 4. Conclusions

Binary/bidisperse suspensions have received significant scientific interest, not only because of their industrial relevance, but because the mechanism by which rheological modification is achieved remains to be debated. A binary suspension of $Mg(OH)_2$ and nano-$SiO_2$ was studied to understand how yield stress could be reduced by adding small amounts of nano-$SiO_2$. The system is particularly relevant to the processing of intermediate-level nuclear waste in the UK, which is predominantly magnesium hydroxide. Being able to reduce yield stress but maintain a high solids content is favorable for processing and encapsulation of the waste for long-term storage.

Adding nano-$SiO_2$ at an approximately equivalent number ratio to $Mg(OH)_2$, the yield stress of the binary suspension was reduced by almost 50 % compared to the $Mg(OH)_2$ suspension. X-ray CT imaging revealed that approximately two-thirds of the 3 vol% nano-$SiO_2$ added to the $Mg(OH)_2$ suspension was well-dispersed, with the rest forming large clusters that had minimal interaction with the $Mg(OH)_2$ network. SEM images showed small aggregates/individual particles of nano-$SiO_2$ dispersed between $Mg(OH)_2$ particles. We conclude that the finely dispersed nano-$SiO_2$ act as ball bearings to lubricate contacts between the irregularly shaped $Mg(OH)_2$ particles, thus decreasing yield stress. The ball bearing lubrication mechanism provides new insight into achieving rheological modification with few secondary particles dispersed and distributed throughout the $Mg(OH)_2$ network. The mechanism differs from other proposed mechanisms (particle coatings to modify electrostatic interactions, nanoparticle 'haloing' of the larger particles, and deviated stress distribution via the smaller particle network) which rely on more contribution from the secondary particles.

A side effect of this particular binary suspension is the reaction between soluble $Si(OH)_4$ and $Mg^{2+}$ to form magnesium silicate hydrate (MSH). The MSH precipitates onto the nano-$SiO_2$ to fuse particles together, thus reducing their effectiveness as flow modifiers and increasing the suspension yield stress. However, the reaction kinetics are sufficiently slow that any impact on the processability of the material (for the nuclear application) would be negligible.

The practical benefit of decreasing yield stress is that higher solids content suspensions of nuclear waste can be processed and encapsulated for long-term storage. Since the volume of waste to be stored is significant, any improvement in solid content loading will considerably reduce the total number of waste packages stored, which is not only an economic benefit, but more crucially reduces the hazard of storing the nuclear waste.

## Supporting information

S1 Particle shape analysis; S2 Particle zeta potential and size distribution; S3 UV–vis silica standard calibration.

## CRediT authorship contribution statement

**David Harbottle:** Writing – review & editing, Writing – original draft, Supervision, Resources, Methodology, Funding acquisition, Formal analysis, Conceptualization. **Timothy N. Hunter:** Writing – review & editing, Supervision, Resources, Investigation, Formal analysis. **Vyacheslav Kachkanov:** Writing – review & editing, Investigation, Formal analysis, Conceptualization. **Leonard Turpin:** Writing – review & editing, Investigation, Formal analysis, Conceptualization. **Olivia Pickup:** Writing – original draft, Methodology, Investigation, Formal analysis, Data curation. **Alexander Lockwood:** Writing – review & editing, Supervision, Investigation, Funding acquisition. **Martyn Barnes:** Writing – review & editing, Supervision, Funding acquisition, Formal analysis. **Ria Mitchell:** Writing – review & editing, Investigation, Formal analysis.

## Declaration of Competing Interest

The authors declare that they have no known competing financial interests or personal relationships that could have appeared to influence the work reported in this paper.

## Data Availability

The data associated with this paper are openly available from the University of Leeds Data Repository. http://doi.org/10.5518/1517

## Acknowledgements

This research was completed at the EPSRC Centre for Doctoral Training in Nuclear Energy – GREEN (Growing skills for Reliable Economic Energy from Nuclear) (EP/S022295/1), in collaboration with Sellafield Ltd., who the authors greatly acknowledge for their technical input and financial support of this work. We would also like to acknowledge the allocation of the synchrotron X-ray beamtime at the Diamond-Manchester Imaging beamline (I13–2) at the Diamond Light Source, UK (MG32814). Authors acknowledge the University of Sheffield Tomography Centre (STC) funding from EPSRC (EP/T006390/1).

## Appendix A. Supporting information

Supplementary data associated with this article can be found in the online version at doi:10.1016/j.colsurfa.2024.134062.

## References

[1] D.V. Boger, Rheology and the resource industries, Chem. Eng. Sci. 64 (2009) 4525–4536.
[2] A. Nasu, Y. Otsubo, Rheology and UV protection properties of suspensions of fine titanium dioxides in a silicone oil, J. Colloid Interface Sci. 296 (2006) 558–564.
[3] T. Xu, Y. Cai, K.E. O'Shea, Adsorption and photocatalyzed oxidation of methylated arsenic species in TiO2 suspensions, Environ. Sci. Technol. 41 (2007) 5471–5477.
[4] J.J. Hastings, D. Rhodes, A.S. Fellerman, D. McKendrick, C. Dixon, New approaches for sludge management in the nuclear industry, Powder Technol. 174 (2007) 18–24.
[5] M. Johnson, M. Fairweather, D. Harbottle, T.N. Hunter, J. Peakall, S. Biggs, Yield stress dependency on the evolution of bubble populations generated in consolidated soft sediments, AIChE J. 63 (2017) 3728–3742.
[6] M. Johnson, J. Peakall, X. Jia, M. Fairweather, D. Harbottle, S. Biggs, T.N. Hunter, Enhanced gas migration through permeable bubble networks within consolidated soft sediments, AIChE J. 64 (2018) 4131–4147.
[7] M. Johnson, J. Peakall, M. Fairweather, M. Barnes, S. Davison, X. Jia, M.A. Clare, D. Harbottle, T.N. Hunter, Sediment microstructure and the establishment of gas migration pathways during bubble growth, Environ. Sci. Technol. 53 (2019) 12882–12892.
[8] T.N. Hunter, J. Peakall, D. Egarr, D.M.J. Cowell, S. Freear, A.S. Tonge, L. Horton, H.P. Rice, I. Smith, K. Malone, D. Burt, M. Barnes, G. Randall, S. Biggs, M. Fairweather, Concentration profiling of a horizontal sedimentation tank utilising a bespoke acoustic backscatter array and CFD simulations, Chem. Eng. Sci. 218 (2020) 115560.
[9] A.P.G. Lockwood, J. Peakall, N.J. Warren, G. Randall, M. Barnes, D. Harbottle, T. N. Hunter, Structure and sedimentation characterisation of sheared Mg(OH)2 suspensions flocculated with anionic polymers, Chem. Eng. Sci. 231 (2021) 116274.
[10] J. Gustafsson, P. Mikkola, M. Jokinen, J.B. Rosenholm, The influence of pH and NaCl on the zeta potential and rheology of anatase dispersions, Colloids Surf. A: Physicochem. Eng. Asp. 175 (2000) 349–359.
[11] Z. Zhou, P.J. Scales, D.V. Boger, Chemical and physical control of the rheology of concentrated metal oxide suspensions, Chem. Eng. Sci. 56 (2001) 2901–2920.
[12] S.B. Johnson, G.V. Franks, P.J. Scales, D.V. Boger, T.W. Healy, Surface chemistry–rheology relationships in concentrated mineral suspensions, Int. J. Miner. Process. 58 (2000) 267–304.
[13] Y.-K. Leong, D.V. Boger, Surface chemistry effects on concentrated suspension rheology, J. Colloid Interface Sci. 136 (1990) 249–258.
[14] Y.-K. Leong, P.J. Scales, T.W. Healy, D.V. Boger, Effect of particle size on colloidal zirconia rheology at the isoelectric point, J. Am. Ceram. Soc. 78 (1995) 2209–2212.
[15] J.A. Yanez, T. Shikata, F.F. Lange, D.S. Pearson, Shear modulus and yield stress measurements of attractive alumina particle networks in aqueous slurries, J. Am. Ceram. Soc. 79 (1996), 2917-2917.
[16] B. Wolf, W.J. Frith, S. Singleton, M. Tassieri, I.T. Norton, Shear behaviour of biopolymer suspensions with spheroidal and cylindrical particles, Rheol. Acta 40 (2001) 238–247.
[17] S. Biggs, R. Nabi, C. Poole, A. Patel, The Influence of Zeta Potential and Yield Stress on the Filtration Characteristics of a Magnesium Hydroxide Simulant, 2007, pp. 1133-1139.
[18] Y.-K. Leong, D.V. Boger, P.J. Scales, T.W. Healy, R. Buscall, Control of the rheology of concentrated aqueous colloidal systems by steric and hydrophobic forces, J. Chem. Soc. Chem. Commun. (1993) 639–641.
[19] S. Zhang, N. Sha, Z. Zhao, Surface modification of α-Al2O3 with dicarboxylic acids for the preparation of UV-curable ceramic suspensions, J. Eur. Ceram. Soc. 37 (2017) 1607–1616.
[20] P.S. Bhosale, J.C. Berg, Poly(acrylic acid) as a rheology modifier for dense alumina dispersions in high ionic strength environments, Colloids Surf. A: Physicochem. Eng. Asp. 362 (2010) 71–76.
[21] C. Corkhill, N. Hyatt, Nuclear Waste Management, IOP Publishing, 2018.
[22] N.C. Hyatt, M.I. Ojovan, Special issue: materials for nuclear waste immobilization, Materials 12 (2019).
[23] M. Cerbelaud, A. Videcoq, P. Abélard, C. Pagnoux, F. Rossignol, R. Ferrando, Heteroaggregation between Al2O3 submicrometer particles and SiO2 nanoparticles: experiment and simulation, Langmuir 24 (2008) 3001–3008.
[24] M. Cerbelaud, A. Videcoq, F. Rossignol, M.A. Piechowiak, D. Bochicchio, R. Ferrando, Heteroaggregation of ceramic colloids in suspensions, Adv. Phys.: X 2 (2017) 35–53.
[25] A. Aimable, A. Delomenie, M. Cerbelaud, A. Videcoq, T. Chartier, F. Boutenel, T. Cutard, G. Dusserre, An experimental and simulation study of heteroaggregation in a binary mixture of alumina and silica colloids, Colloids Surf. A: Physicochem. Eng. Asp. 605 (2020) 125350.
[26] M. Cerbelaud, M. Muñoz, F. Rossignol, A. Videcoq, Self-organization of large alumina platelets and silica nanoparticles by heteroaggregation and sedimentation: toward an alternative shaping of nacre-like ceramic composites, Langmuir 36 (2020) 3315–3322.
[27] A. Singh, C. Ness, A.K. Sharma, J.J. de Pablo, H.M. Jaeger, Rheology of bidisperse non-Brownian suspensions, arXiv, 2023.
[28] M.L. Fisher, M. Colic, M.P. Rao, F.F. Lange, Effect of silica nanoparticle size on the stability of alumina/silica suspensions, J. Am. Ceram. Soc. 84 (2001) 713–718.
[29] C. Wu, L. Wang, D. Harbottle, J. Masliyah, Z. Xu, Studying bubble–particle interactions by zeta potential distribution analysis, J. Colloid Interface Sci. 449 (2015) 399–408.
[30] X. Zhu, D. Jiang, S. Tan, Z. Zhang, Dispersion properties of alumina powders in silica sol, J. Eur. Ceram. Soc. 21 (2001) 2879–2885.
[31] D. Kong, H. Yang, Y. Yang, S. Wei, J. Wang, B. Cheng, Dispersion behavior and stabilization mechanism of alumina powders in silica sol, Mater. Lett. 58 (2004) 3503–3508.
[32] A.J.W. ten Brinke, L. Bailey, H.N.W. Lekkerkerker, G.C. Maitland, Rheology modification in mixed shape colloidal dispersions. Part II: mixtures, Soft Matter 4 (2008) 337–348.
[33] Q.D. Nguyen, D.V. Boger, Measuring the flow properties of yield stress fluids, Annu. Rev. Fluid Mech. 24 (1992) 47–88.
[34] M. Dinkgreve, J. Paredes, M.M. Denn, D. Bonn, On different ways of measuring "the" yield stress, J. Non-Newton. Fluid Mech. 238 (2016) 233–241.
[35] H. Yang, C. Li, C. Wei, M. Li, X. Li, Z. Deng, G. Fan, Molybdenum blue photometry method for the determination of colloidal silica and soluble silica in leaching solution, Anal. Methods 7 (2015) 5462–5467.
[36] J.D.H. Strickland, The preparation and properties of silicomolybdic acid. I. The properties of alpha silicomolybdic acid, J. Am. Chem. Soc. 74 (1952) 862–867.
[37] E.A. Nagul, I.D. McKelvie, P. Worsfold, S.D. Kolev, The molybdenum blue reaction for the determination of orthophosphate revisited: opening the black box, Anal. Chim. Acta 890 (2015) 60–82.
[38] N. Wadeson, M. Basham, Savu: A Python-based, MPI Framework for Simultaneous Processing of Multiple, N-dimensional, Large Tomography Datasets.
[39] R. Hogg, T.W. Healy, D.W. Fuerstenau, Mutual coagulation of colloidal dispersions, Trans. Faraday Soc. 62 (1966) 1638–1651.
[40] T. Athar, Chapter 17 - Smart precursors for smart nanoparticles, in: W. Ahmed, M. J. Jackson (Eds.), Emerging Nanotechnologies for Manufacturing (Second Edition), William Andrew Publishing, Boston, 2015, pp. 444–538.
[41] J.A. Botha, W. Ding, T.N. Hunter, S. Biggs, G.A. Mackay, R. Cowley, S. E. Woodbury, D. Harbottle, Quartz crystal microbalance as a device to measure the yield stress of colloidal suspensions, Colloids Surf. A: Physicochem. Eng. Asp. 546 (2018) 179–185.
[42] J. Schaefer, E.H.G. Backus, M. Bonn, Evidence for auto-catalytic mineral dissolution from surface-specific vibrational spectroscopy, Nat. Commun. 9 (2018) 3316.
[43] J. Temuujin, K. Okada, K.J.D. MacKenzie, Formation of layered magnesium silicate during the aging of magnesium hydroxide–silica mixtures, J. Am. Ceram. Soc. 81 (1998) 754–756.
[44] S.A. Walling, H. Kinoshita, S.A. Bernal, N.C. Collier, J.L. Provis, Structure and properties of binder gels formed in the system Mg(OH)2–SiO2–H2O for immobilisation of magnox sludge, Dalton Trans. 44 (2015) 8126–8137.

[45] C. Dewitte, A. Bertron, M. Neji, L. Lacarrière, A. Dauzères, Chemical and microstructural properties of designed cohesive M-S-H pastes, Materials 15 (2022).

[46] T. Zhang, J. Zou, B. Wang, Z. Wu, Y. Jia, C.R. Cheeseman, Characterization of magnesium silicate hydrate (MSH) gel formed by reacting MgO and silica fume, Mater. (Basel) 11 (2018) 909.

[47] S. Kumar, J. Lei, E.-H. Yang, C. Unluer, Influence of different additives on the rheology and microstructural development of MgO–SiO2 mixes, Compos. Part B: Eng. 235 (2022) 109784.

[48] N. Roussel, G. Ovarlez, S. Garrault, C. Brumaud, The origins of thixotropy of fresh cement pastes, Cem. Concr. Res. 42 (2012) 148–157.

[49] T. Zhang, T. Li, Z. Zhou, M. Li, Y. Jia, C. Cheeseman, A novel magnesium hydroxide sulfate hydrate whisker-reinforced magnesium silicate hydrate composites, Compos. Part B: Eng. 198 (2020) 108203.

[50] C. Roosz, S. Grangeon, P. Blanc, V. Montouillout, B. Lothenbach, P. Henocq, E. Giffaut, P. Vieillard, S. Gaboreau, Crystal structure of magnesium silicate hydrates (M-S-H): the relation with 2:1 Mg–Si phyllosilicates, Cem. Concr. Res. 73 (2015) 228–237.

[51] Y. Nishiki, J. Cama, T. Otake, R. Kikuchi, M. Shimbashi, T. Sato, Formation of magnesium silicate hydrate (M-S-H) at pH 10 and 50°C in open-flow systems, Appl. Geochem. 148 (2023) 105544.